AIP | Review of Scientific Instruments

Magnetic bucket for rotating unmagnetized plasma

Noam Katz, Cami Collins, John Wallace, Mike Clark, David Weisberg et al.

Citation: Rev. Sci. Instrum. **83**, 063502 (2012); doi: 10.1063/1.4723820
View online: http://dx.doi.org/10.1063/1.4723820
View Table of Contents: http://rsi.aip.org/resource/1/RSINAK/v83/i6
Published by the American Institute of Physics.

Additional information on Rev. Sci. Instrum.

Journal Homepage: http://rsi.aip.org
Journal Information: http://rsi.aip.org/about/about_the_journal
Top downloads: http://rsi.aip.org/features/most_downloaded
Information for Authors: http://rsi.aip.org/authors

ADVERTISEMENT

Downloaded 24 Apr 2013 to 128.104.166.218. This article is copyrighted as indicated in the abstract. Reuse of AIP content is subject to the terms at: http://rsi.aip.org/about/rights_and_permissions

Magnetic bucket for rotating unmagnetized plasma

Noam Katz,[a] Cami Collins, John Wallace, Mike Clark, David Weisberg, Jon Jara-Almonte, Ingrid Reese, Carl Wahl, and Cary Forest
Department of Physics, University of Wisconsin, Madison, Wisconsin 53706, USA

(Received 26 February 2012; accepted 14 May 2012; published online 1 June 2012)

A new experiment is described which generates flow in unmagnetized plasma. Confinement is provided by a cage of permanent magnets, arranged to form an axisymmetric, high-order, multipolar magnetic field. This field configuration—sometimes called a "magnetic bucket"—has a vanishingly small field in the core of the experiment. Toroidal rotation is driven by $\mathbf{J} \times \mathbf{B}$ forces applied in the magnetized edge. The cross-field current that is required for this forcing flows from anodes to thermionic cathodes, which are inserted between the magnet rings. The rotation at the edge reaches 3 km/s and is viscously coupled to the unmagnetized core plasma. We describe the conditions necessary for rotation, as well as a 0-dimensional power balance used to understand plasma confinement in the experiment. © *2012 American Institute of Physics*. [http://dx.doi.org/10.1063/1.4723820]

I. INTRODUCTION

This article describes a newly constructed experiment which combines the concept of a magnetic bucket with $\mathbf{J} \times \mathbf{B}$ forcing; the result is a spinning unmagnetized plasma suitable for both astrophysically relevant studies and centrifugal gas separation.

This experiment is ideal for studying astrophysical phenomena—such as the dynamo process[1] and the magneto-rotational instability (MRI) (Ref. 2)—in which the flow energy, rather than the magnetic energy, drives the relevant instabilities. Previous experiments[3] relied on rotating liquid metals, which can be stirred mechanically and need no magnetic field for confinement. However, these experiments suffer from several drawbacks. The characteristic rotation velocity, V, is limited, and therefore the magnetic Reynolds number $Rm = VL/\eta$ (where L is the characteristic size, and η is the resistivity) is typically less than $\sim$100; this value is barely large enough to reach the critical Rm for dynamo and MRI excitation. In addition, the fluid Reynolds number, $Re = VL/\nu$ (where ν is the viscosity), cannot be varied independently of Rm in liquid metals; the ratio of these quantities $Pm = Rm/Re = \nu/\eta$ is fixed, and the flow is always turbulent. In contrast, in a plasma the achievable rotation velocities are large, and Rm can be varied independently of Re by changing the electron temperature. Therefore, a rotating unmagnetized plasma is the ideal system for exploring astrophysical phenomena over a large range of Rm and Re.

Another possible application of a spinning unmagnetized plasma is for separation of ions by mass. Plasma centrifuges have been proposed and built before (e.g., Refs. 4–6), but their confinement always relied on large magnetic fields throughout the plasma volume. In the present apparatus, the magnetic field needs only be large at the edge, potentially offering significant cost reduction. Moreover, since this field is due to permanent magnets, no power is required to maintain it.

The idea of using multicusp, or multipole magnetic fields of permanent magnets to confine a plasma has existed for at least 40 years.[7] The loss area is reduced to a thin strip associated with mirror losses, and the configuration results in a large volume of uniform, unmagnetized plasma, which is potentially steady-state. We enhance this basic confinement scheme by driving poloidal currents across the magnetized plasma edge. Because our permanent magnets are arranged to provide purely poloidal field, the resulting $\mathbf{J} \times \mathbf{B}$ force drives strong toroidal rotation.

Initial results showing plasma rotation have previously been reported in Ref. 8; here, we present additional data and describe the apparatus in more detail. Section II describes the setup of the experiment, while Sec. III describes the $\mathbf{J} \times \mathbf{B}$ rotation drive. We study confinement in Sec. IV using a simple model for the particle and energy balance; we then use this model to calculate the obtainable range of Re and Rm values. Section V contains results of rotation velocity measurements in helium, and Sec. VI contains concluding remarks.

II. EXPERIMENTAL APPARATUS

Figure 1 shows the permanent magnet assembly which provides plasma confinement. The cylindrical, ceramic magnets (B=0.15 T at magnet surfaces) are glued to a ring-shaped, stainless steel ribbon with high-temperature epoxy; copper water-cooling lines run along the back of this stainless ribbon, while the fronts of the magnets are covered with aluminum limiters. The limiters were plasma-sprayed with alumina at Thermal Spray Technologies, Inc. to provide an electrically insulating boundary condition and protect the magnets from heating by mirror-lost particles. The alumina has survived nearly 100 h of accumulated run-time, although it shows a large dark band along its center due to plasma bombardment and deposition.

The magnet rings are arranged in a stack, separated by 2.5″ vertically, with the field of each ring pointing opposite that of its neighboring rings. The top and bottom are also bounded by magnet rings, whose radial separation is 2″. The magnets in each ring all point in the same direction (inward or outward). Figure 1 also shows a central column of magnets,

[a]nkatz2@wisc.edu.

 © 2012 American Institute of Physics

Downloaded 24 Apr 2013 to 128.104.166.218. This article is copyrighted as indicated in the abstract. Reuse of AIP content is subject to the terms at: http://rsi.aip.org/about/rights_and_permissions

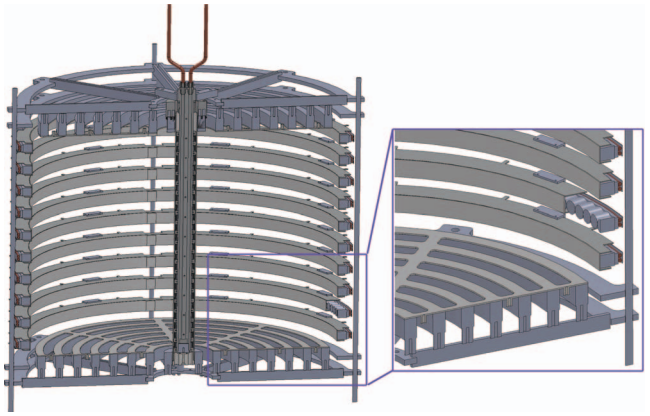

FIG. 1. Left: permanent magnet cage for confining unmagnetized plasma. Adjacent rings have oppositely oriented magnetic field. Right: zoomed-in view of a magnet ring, with limiter pulled back to reveal individual ceramic magnets. Also visible are cooling lines behind the magnets. The limiters, which are made of aluminum and coated with insulating alumina, have so far been installed only on the side magnet rings. Quartz tape covers the top and bottom rings, while a quartz tube covers the central column. The entire magnet assembly is placed inside a vacuum vessel.

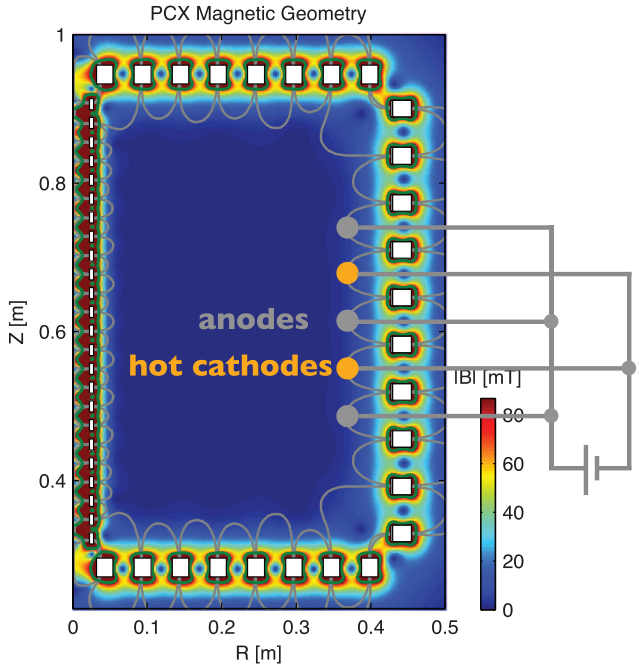

FIG. 2. Magnetic field amplitude shown in poloidal cross-section; white squares indicate magnet rings. Dark green curve near magnets shows electron cyclotron resonance location. Superimposed at right are the stirring electrodes. Reproduced by permission from Collins *et al.*, Phys. Rev. Lett. **108**, 115001 (2012). Copyright (2012) by the American Physical Society.

which defines the inner plasma boundary, and will be used to achieve Couette rotation (sheared flow between two cylinders). These magnets are single-piece NdFeB rings (Br_{max} = 11,900 Gauss, BH_{max} = 35 MGOe), with vertical separation of 1″. The field at their surface is 0.23 T. The arrangement of magnets with alternating polarity in adjacent rings ensures a vanishingly small magnetic field in the bulk of the experiment (see Fig. 2).

It is important to note the differences between our magnetic bucket, which has axisymmetric magnet rings, and other such experiments where the magnets are arranged in non-axisymmetric grids or vertical lines (e.g., see Refs. 7 and 9). In our axisymmetric geometry, the ∇B and curvature drifts are toroidal and serve to equilibrate the potential in this direction. This allows us to use toroidally localized electrodes, which then form "virtual" axisymmetric electrodes. Another important difference from previous magnetic buckets is the use of insulating boundaries at the magnet faces. The insulating limiters are crucial for plasma rotation, since they allow for an electric field to be applied across the magnetic field without shorting out.

The vacuum is provided by a cryopump (CTI-Cryogenics Cryo-Torr 8) and a turbomolecular pump (Varian Macro-Torr 1000HT Turbo-V). We bake the outer vessel to about 50°C and the magnets to about 40°C by pumping initially room-temperature water through the cooling lines. The base pressure after baking is near 5×10^{-7} torr, and falls by a factor of 2 once the magnets are cooled to 20°C. The pressure is measured by a Penning cold-cathode gauge. The gases we use are helium and argon back-filled to pressures of $10^{-6} - 10^{-4}$ torr.

We use a 6 kW, 2.45 GHz Cober magnetron to provide electron cyclotron heating, which both breaks down the gas and sustains the plasma. Since the bulk of the chamber is unmagnetized, the resonance location (where B = 87.5 mT) occurs very close to the magnet rings. The location of the resonance is indicated in Fig. 2 by a dark green line. As shown in the figure, the stronger magnets of the center column have a continuous resonance surface—in contrast with the ceramic magnets—and this surface is farther away from the inner boundary. The microwave horn is a WR-284 waveguide, cut off to be flush with the plasma-facing surfaces of the side magnet rings. Because the horn is less than a microwave wavelength away from the plasma, an E-H tuner is necessary to match the impedance of the plasma and reduce the reflected power. The tuning depends on neutral pressure, plasma density, plasma temperature, and vacuum condition, and has to be optimized as these quantities change. The face of the microwave horn is covered by a corrugated boron-nitride plate in order to prevent the plasma from expanding into the waveguide. The corrugation prevents the formation of a conducting path across the face of the waveguide which can form due to plasma deposition.

The microwaves encounter a time-varying neutral pressure—shown in Fig. 3. Initially a high neutral pressure is required for repeatable gas breakdown, while the final low neutral pressure is required for fast rotation.[8] We use a piezo puff valve to achieve the initial peak in the neutral pressure (subfigure (a)), and the gas is then pumped out over the course of the discharge. The plasma is heated throughout the discharge, not only by the electron cyclotron waves, but also by the ohmic heating associated with the rotation electrodes. Consequently, as the density decreases, the electron temperature increases during the discharge. The decreasing density results in increasing anode voltage (subfigure (c)) since the anode area is small and a stronger sheath develops around the anodes. Note that the anode voltage is measured with respect to the grounded chamber wall. Figure 3(d) shows that there is

Downloaded 24 Apr 2013 to 128.104.166.218. This article is copyrighted as indicated in the abstract. Reuse of AIP content is subject to the terms at: http://rsi.aip.org/about/rights_and_permissions

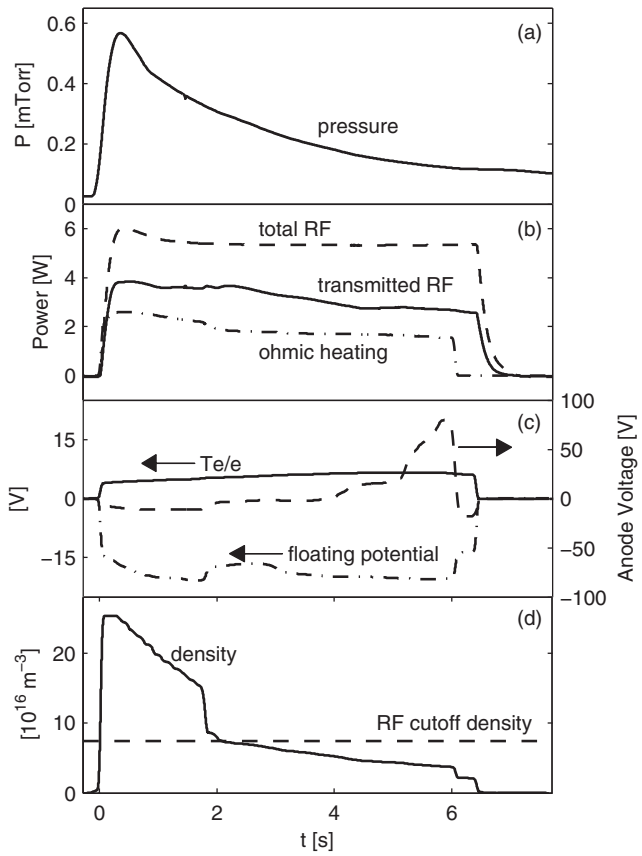

FIG. 3. Typical discharge parameters as a function of time for helium: (a) neutral pressure; (b) electron cyclotron RF heating power and ohmic heating associated with rotation drive (transmitted RF is part of magnetron output that is not reflected); (c) bulk electron temperature and floating potential measured by triple probe, and anode voltage (axis at right); and (d) bulk plasma density measured by triple probe, as well as density at which the 2.45 GHz O-mode is cut off.

a change at $t = 2$ when the plasma transitions from over- to under-dense.

The density and temperature profiles are flat in the bulk plasma (see Fig. 3 in Ref. 8); at the transition from over- to under-dense, these quantities change throughout the plasma. The relatively rapid loss of density is related to the sudden change in absorbed power and the relatively short confinement time of $nT_eVol/P_{\text{heating}} \sim 10\ \mu$s. This last quantity is the stored plasma energy divided by the heating power; *Vol* is the plasma volume.

The heating is switched off after 7 s in order to protect the permanent magnets from over-heating and demagnetizing. In addition, as the temperature of the magnets increases (up to 30–40°C) impurity outgassing increases, and the discharge no longer consists of pure noble gas.

The time-scale for changes to the bulk plasma parameters is on the order of seconds, and this time-scale is much longer than the time-scales of interest in the experiment. Specifically, the viscous time for flow equilibration is on the order of $L^2/\nu \sim Re/\Omega \sim 10^{-3}$–$10^{-4}$ s, while the growth rate of the MRI is on the order of $\Omega \sim 10^{-4}$ s, where $\Omega \equiv V/L$ is the angular frequency for rotation, and L is the major radius of the magnet cage. The variations in plasma density and temperature can therefore be neglected over the short time-scales of interest.

The plasma properties are measured by internal probes, as well as by optical diagnostics. There are Mach and Langmuir probes which scan radially at the mid-plane and vertically near the outer magnets. In addition, there is a triple probe about 6 cm above the bottom magnets at mid-radius, which measures density, temperature, and floating potential in the bulk plasma. An Ocean spectrometer, model USB2000+, provides line-integrated spectra, and scans from the center to the outer wall at the mid-plane.

III. ROTATION DRIVE

Plasma rotation is driven by $\mathbf{J} \times \mathbf{B}$ forces in the magnetized edge region and couples into the bulk plasma by collisional viscosity. In order for this drive to be effective, the current has to be large enough, the electrode position must be optimized, and the neutral pressure must be low enough for ion viscosity to dominate the momentum transport to the bulk plasma.

We find that thermionic cathodes are crucial for driving sufficient current across the edge magnetic field. Originally, we installed axisymmetric molybdenum-coated rings for both anodes and cathodes; however, the large area of these rings severely increased the particle losses, and the edge currents were about 10 times too small.[8] We therefore use thoriated tungsten cathodes and molybdenum anodes to drive up to 5 A of current across the face of each magnet ring. This electrode assembly is toroidally localized. However, the single particle drifts (∇B and curvature) are in the toroidal direction, and these serve to symmetrize the potential. Indeed, we measure large plasma rotation toroidally opposite from the driving electrodes.

The cathodes are made from 1% thoriated tungsten wire of diameter 0.38 mm. We find empirically that this diameter is ideal since thinner wires fail too quickly, while thicker wires require too much heating current to be practical. The wires are wound into 1 cm-diameter coils and each leg is attached by press-fit between a copper lead and its surrounding alumina tube. Two coils with total wire length of 40 cm are placed between every other magnet ring along the outer wall. We apply about 11 A of heating current per coil and bring the coils up to 1700°C (measured by a Mikron infrared pyrometer, model M90-V). The anodes are constructed from 1″-long cylinders of 1/2″-diameter molybdenum. The cathodes are biased 400–500 V below the anodes, and the entire electrode assembly is floating relative to ground (the chamber wall). Nevertheless, the anode voltage is typically near ground (Fig. 3(c)). For the data shown in this article, we use only 2 cathodes and 3 anodes at the outer edge (see Fig. 2).

The electrode current—and therefore the plasma rotation—may be limited by several factors. First, the cathode may not be hot enough to emit sufficient electrons. Thermionic cathodes are described by the Richardson-Dushman equation $J = AT^2e^{-W/T}$, where $A = 3 \times 10^4$ A/m^2/K^2 and the work function is $W = 2.63$ eV for thoriated tungsten.[10] There is large uncertainty in these numbers because of possible patchiness in wire composition, but nevertheless it is likely that our current is indeed limited by cathode temperature. There are additional factors that may

Downloaded 24 Apr 2013 to 128.104.166.218. This article is copyrighted as indicated in the abstract. Reuse of AIP content is subject to the terms at: http://rsi.aip.org/about/rights_and_permissions

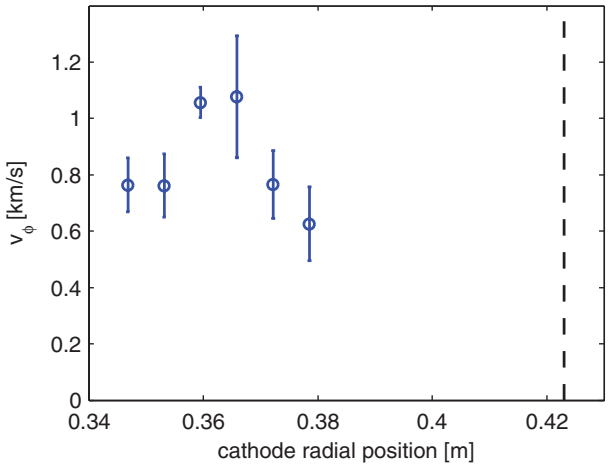

FIG. 4. Measured rotation velocity in helium at fixed radius (R = 0.35 m) as a function of cathode radial position; dashed line represents outer magnets. The fastest rotation is achieved at intermediate cathode position. Anode position is fixed at R = 0.35 m, a value chosen through a similar optimization process. Error bars represent fluctuations about a linear fit of measured velocity vs. time.

limit the current: if the anode area is too small, the anodes may only collect electron saturation current; similarly, if the cathode area is too small or the Debye length too large, the current may be limited by the space-charge potential.

The value of the plasma potential plays an important role in determining the electrode current, and this potential depends on the anode and cathode areas, whether the anodes are grounded, and other charge sinks such as probe surfaces. These dependencies are still under investigation.

As shown in Fig. 4, the plasma rotation depends strongly on the electrode placement. The straight-forward reason for this is that $\mathbf{J} \times \mathbf{B}$ falls quickly to 0 as the electrodes are moved into the unmagnetized core. This change occurs over only a few cm. However, as the electrodes are pulled out and B increases, the cross-field current J decreases. Therefore, the first consideration is to find the intermediate position which maximizes this $\mathbf{J} \times \mathbf{B}$ force. Another reason for the importance of electrode placement involves the perpendicular ion viscosity, which according to Braginskii[11] may be written as

$$\frac{\eta_1}{m_i n} = v_{ti}^2 \tau_i \frac{\frac{24}{5}x^2 + 2.23}{16x^4 + 16.12x^2 + 2.33} = \begin{cases} 0.96 v_{ti}^2 \tau_i, & x \ll 1 \\ \frac{3}{10} v_{ti}^2 \tau_i / x^2, & x \gg 1, \end{cases} \quad (1)$$

where v_{ti} is the ion thermal speed, τ_i is the ion-ion collision time, $x = \omega_{ci}\tau_i$ is the magnetization parameter, and ω_{ci} is the ion cyclotron frequency. The important point is that the unmagnetized viscosity ($x \ll 1$) is much larger than the magnetized viscosity ($x \gg 1$), while between these two limits the viscosity is monotonic with x. In order for the momentum to couple from the magnetized edge into the bulk plasma, the electrodes must be in a region with sufficiently low magnetic field so that the viscosity is large enough. A final consideration for electrode placement involves the electron cyclotron resonance (marked by the dark green contour in Fig. 2). The electrodes and their leads must be protected from this resonant zone where most of the microwave power gets deposited. This is not an issue for our relatively weak outer-wall magnets, but may affect the electrode placement at the inner wall where the magnets are stronger.

IV. POWER BALANCE

In this section, we enumerate the sources and sinks for both particles and energy, and construct a 0-dimensional model for the relationship involving heating power, plasma density, neutral density, and electron temperature. Although the rotation electrodes introduce additional heating power and may affect the plasma potential, we ignore them for simplicity.

We begin with particle balance,[12] which requires that electrons and ions be lost at the same rate. The loss area is assumed to be the same for both species, since we take infinitesimal Debye length. Note that because the magnet faces are insulating, the mirror losses must be identical for ions and electrons.

$$\Gamma \equiv \frac{1}{4} n \sqrt{\frac{8}{\pi}\frac{T_e}{m_e}} \exp\left(-\frac{e\Delta V}{T_e}\right) = \exp\left(-\frac{1}{2}\right) n \sqrt{\frac{T_e}{m_i}}$$

This condition sets the plasma potential:

$$V_p - V_{\text{cusp}} \equiv \Delta V = \frac{T_e}{e}\left(\log\sqrt{\frac{m_i}{2\pi m_e}} + \frac{1}{2}\right). \quad (2)$$

Table I lists the power loss mechanisms for the plasma. The ions lost to the cusps carry not only their thermal energy, but also the energy they gain as they fall through the potential difference between the plasma and the cusp (Eq. (2)). This gained energy is much larger than the initial ion thermal energy. The effective cusp area for plasma losses, which is used in calculating ion power losses, is not well-understood, and empirically is different for fast electrons and for bulk plasma species;[12] here, we take the loss width to be $4\sqrt{\rho_i \rho_e}$, proportional to the geometric mean of the ion and electron gyroradii at the magnet faces. As each ion is lost, we assume there must be a new ionization to replace it and keep the density constant; each ionization reduces the plasma's stored energy by E_{ioniz}. Power may also be lost due to ion and neutral radiation. The radiation coefficients associated with these processes, $M(T_e)$ and $R^i(T_e)$, were provided by Dennis Whyte using the KPRAD code.[13]

TABLE I. Power loss mechanisms in magnetic bucket. A_{cusp} is the effective loss area at the magnetic cusps; $M(T_e)$ is the radiation coefficient for neutral radiation; n_0 is the neutral density; σ_{cx} is the charge-exchange cross-section; Vol is the plasma volume; T_0 is room temperature; and $R^i(T_e)$ is the ion radiation coefficient.

Loss mechanism	Expression [energy/time]
Ion losses at cusps	$\Gamma A_{\text{cusp}}(e\Delta V + \frac{3}{2}T_i)$
Electron losses at cusps	$\Gamma A_{\text{cusp}}(\frac{3}{2}T_e)$
Replacement ionization	$Q_{\text{ioniz}} \equiv \Gamma A_{\text{cusp}} E_{\text{ioniz}}$
Neutral radiation	$M(T_e) Q_{\text{ioniz}}$
Charge-exchange collisions	$\frac{3}{2} n n_0 \langle\sigma_{cx} v\rangle e(T_i - T_0) Vol$
Ion radiation	$n^2 R^i(T_e) Vol$

Downloaded 24 Apr 2013 to 128.104.166.218. This article is copyrighted as indicated in the abstract. Reuse of AIP content is subject to the terms at: http://rsi.aip.org/about/rights_and_permissions

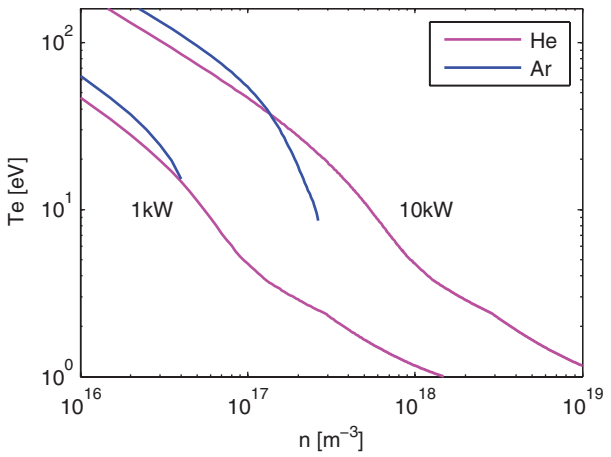

FIG. 5. Power balance calculation for helium and argon with 1 kW of heating power; electron temperature decreases with density. Argon has no solution above certain density because of large radiation power losses.

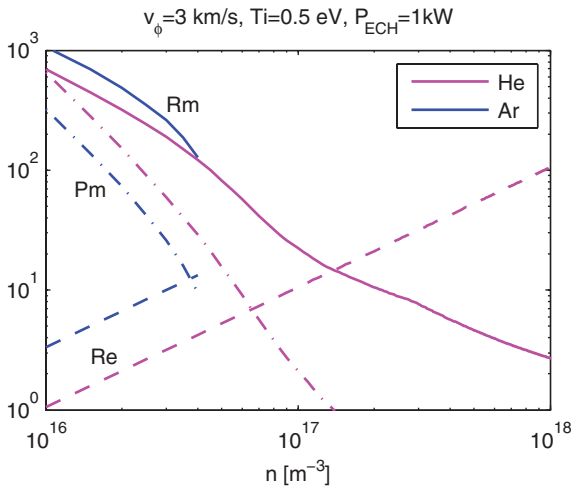

FIG. 6. Power balance calculation of *Rm*, *Re*, and *Pm* as functions of density for 1 kW heating power; *Rm* uses electron temperature from Fig. 5.

The procedure for energy balance is as follows: we start with given density n and heating power and we calculate T_e by setting the heating power equal to the sum of the power losses listed in Table I. We neglect ion radiation and charge exchange losses, and we also ignore T_i in the expression for ion losses at cusps since it is small relative to $e\Delta V$. The results for helium and argon are shown in Fig. 5 for two different heating powers. Comparison with Fig. 3 shows that we must assume only a fraction of the heating power couples to the plasma. For example, in Fig. 3, at $n = 7 \times 10^{16}$ m^{-3}, we measure $T_e = 5$ eV with 4 kW of heating power, similar to the power balance calculation with only 1 kW of heating power (see Fig. 5). In other words, if we assume that only 1/4 of the microwave power couples to the plasma, we are able to account for the electron temperature.

The ion temperature is more difficult to model. Ion power loss is given by the last two terms in Table I, while ions are heated by collisions with electrons and by the combination of ion acceleration through ΔV and ion-ion collisions in the edge region. This last heating mechanism is thought to be the dominant one, but it is not well understood. Instead, we follow Ref. 8 and estimate the ion temperature to be 0.25−0.75 eV.

The implications of this power balance calculation for *Re*, *Rm* and *Pm* are shown graphically in Fig. 6. We take the case of 1 kW heating power and use the results of Fig. 5. It is seen that *Rm* can reach 10^3 at low densities, a value much larger than in liquid metal experiments. In addition, *Pm* can now vary over a large range, as opposed to being fixed at $\sim 10^{-6}$ as in liquid metals. With extra power, the magnetic Reynolds number is expected to reach even higher values, as T_e is increased. This scaling will be tested in an upcoming experiment, which has recently been constructed in Madison.[14]

V. RESULTS

The central result is the demonstration of solid-body rotation of an unmagnetized plasma at speeds approaching 3 km/s at the outer wall. Figure 7 shows that this plasma rotation increases during the discharge as the neutral pressure decreases. Although preliminary results have been reported in Ref. 8, we have since upgraded our data acquisition system and are able

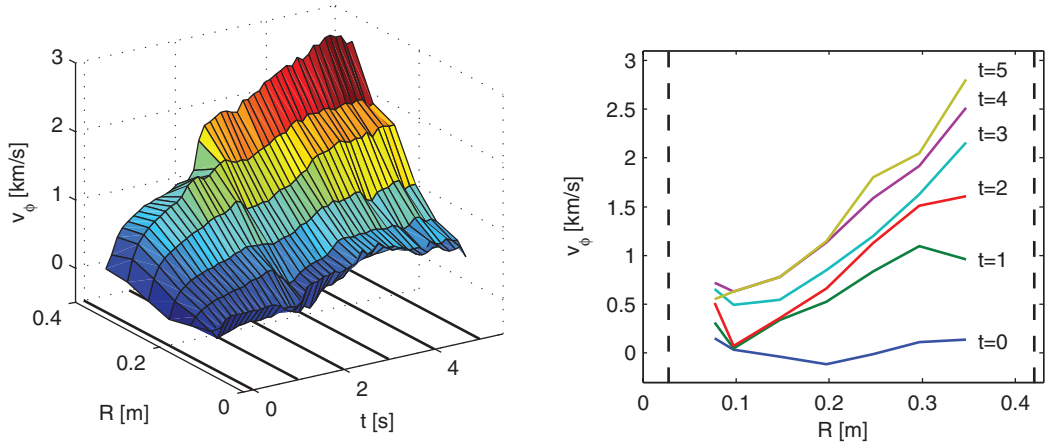

FIG. 7. Left: toroidal velocity measured at the mid-plane in helium plasmas as a function of radius and time; right: velocity profiles at different times corresponding to the black lines in the left-hand subfigure. Rotation is approximately solid-body. A low-pass filter has been applied to remove the 60 Hz component.

Downloaded 24 Apr 2013 to 128.104.166.218. This article is copyrighted as indicated in the abstract. Reuse of AIP content is subject to the terms at: http://rsi.aip.org/about/rights_and_permissions

to record rotation throughout the discharge. The data are combined from several discharges, each with the Mach probe at a different radial position. The cuts in the right-hand subfigure show velocity profiles at different time slices, corresponding to the black lines in the left-hand subfigure. Rotation is approximately solid-body ($v_\phi \propto R$), and increases in time as the discharge changes. In Ref. 8, it was shown that the velocity profile is directly related to the neutral pressure and the Braginskii viscosity. Figure 7 shows data only for helium, but we have successfully rotated argon plasmas as well.

VI. CONCLUSIONS

We have described a new experiment for rotating unmagnetized plasma using $\mathbf{J} \times \mathbf{B}$ forcing in a magnetic bucket configuration. The apparatus is suitable for new astrophysically relevant experiments on flow-driven plasma instabilities as well as centrifugal species separation.

As in previous magnetic buckets, the arrangement of permanent magnets into a multicusp configuration results in a large volume of uniform, unmagnetized plasma. We performed a power balance calculation to show that there is a large range of accessible *Re*, *Rm*, and *Pm*.

Plasma rotation is achieved by the application of poloidal currents across the poloidal magnetic field; the currents are driven using a specially developed electrode system, and the rotation couples to the unmagnetized bulk plasma by ion viscosity. The rotation is fastest when the neutral pressure reaches its lowest point at the end of the discharge.

We are currently developing a cathode system for the central magnet column in order to drive rotation on the inner wall and achieve sheared Couette flow; each cathode will be wired independently for heating and biasing, and the central column will be vertically removable through a gate valve for cathode maintenance.

ACKNOWLEDGMENTS

This work was funded in part by National Science Foundation (NSF) and (U.S.) Department of Energy (DOE). C.C. acknowledges support from the ORISE Fusion Energy Sciences Graduate Fellowship, and N.K. acknowledges support from the ORISE Fusion Energy Sciences Postdoctoral Fellowship. We thank Dennis Whyte for providing the radiation coefficients.

[1] M. Ossendrijver, Astron. Astrophys. Rev. **11**, 287 (2003).
[2] S. A. Balbus and J. F. Hawley, Rev. Mod. Phys. **70**, 1 (Jan. 1998).
[3] A. Gailitis, O. Lielausis, E. Platacis, G. Gerbeth, and F. Stefani, Rev. Mod. Phys. **74**, 973 (2002).
[4] B. W. James and S. W. Simpson, Plasma Phys. **18**, 289 (1976).
[5] T. Ohkawa and R. L. Miller, Phys. Plasmas **9**, 5116 (2002).
[6] A. J. Fetterman and N. J. Fisch, Phys. Plasmas **18**, 094503 (2011).
[7] R. Limpaecher and K. MacKenzie, Rev. Sci. Instrum. **44**, 726 (1973).
[8] C. Collins, N. Katz, J. Wallace, J. Jara-Almonte, I. Reese, E. Zweibel, and C. Forest, Phys. Rev. Lett. **108**, 115001 (2012).
[9] M. Rhodes, J. M. Dawson, J. N. Le Boeuf, and N. C. Luhmann, Phys. Rev. Lett. **48**, 1821 (1982).
[10] E. A. Lederer, in *Vacuum Tube Design* (RCA, 1940), pp. 1–10 .
[11] S. I. Braginskii, Rev. Plasma Phys. **1**, 205 (1965).
[12] M. H. Cho, N. Hershkowtitz, and T. P. Intrator, J. Appl. Phys. **67**, 3254 (1990).
[13] D. G. Whyte, T. E. Evans, A. G. Kellman, D. A. Humphreys, A. W. Hyatt, T. C. Jernigan, R. L. Lee, S. L. Luckhardt, P. B. Parks, M. J. Schaffer, and P. L. Taylor, *Proceedings of the 24th European Conference on Controlled Fusion and Plasma Physics* (Berchtesgaden, Germany, 1997), Vol. 21A, p. 1137.
[14] E. J. Spence, K. Reuter, and C. B. Forest, Astrophys. J. **700**, 470 (2009).

Downloaded 24 Apr 2013 to 128.104.166.218. This article is copyrighted as indicated in the abstract. Reuse of AIP content is subject to the terms at: http://rsi.aip.org/about/rights_and_permissions